Exploiting cationic vacancies for increased energy densities in dual-ion batteries

Toshinari Koketsu, Jiwei Ma, Benjamin J Morgan, Monique Body, Christophe Legein, Pooja Goddard, Olaf Borkiewicz, Peter Strasser, Damien Dambournet

Exploiting Cationic Vacancies for Increased Energy Densities in Dual-Ion Batteries

*Toshinari Koketsu[1], Jiwei Ma[2,3,4], Benjamin. J. Morgan[5], Monique Body[6], Christophe Legein[6], Pooja Goddard[7], Olaf J. Borkiewicz[8], Peter Strasser[1], and Damien Dambournet[2,3]**

[1] The Electrochemical Energy, Catalysis, and Materials Science Laboratory, Department of Chemistry, Technical University Berlin, 10623 Berlin, Germany

[2] Sorbonne Université, CNRS, Physico-chimie des électrolytes et nano-systèmes interfaciaux, PHENIX, F-75005 Paris, France

[3] Réseau sur le Stockage Electrochimique de l'Energie (RS2E), FR CNRS 3459, 80039 Amiens Cedex, France

[4] Institute of New Energy for Vehicles, School of Materials Science and Engineering, Tongji University, Shanghai 201804, China

[5] Department of Chemistry, University of Bath, BA2 7AY Bath, United Kingdom. The Faraday Institution, Quad One, Harwell Science and Innovation Campus, Didcot, UK.

[6] Institut des Molécules et des Matériaux du Mans (IMMM) - UMR 6283 CNRS, Le Mans Université, Avenue Olivier Messiaen, 72085 Le Mans Cedex 9, France.

[7] Department of Chemistry, Loughborough University, Epinal Way, Loughborough LE11 3TU, UK.

[8] X-ray Science Division, Advanced Photon Source, Argonne National Laboratory, Argonne, Illinois, USA.

Keywords: Lithium-magnesium dual ion, defects, DFT-calculations, 7Li and 19F solid-state NMR.

Abstract. Dual-ion Li–Mg batteries offer a potential route to cells that combine desirable properties of both single-ion species. To maximize the energy density of a dual-ion battery, we propose a strategy for achieving simultaneous intercalation of both ionic species, by chemically modifying the intercalation host material to produce a second, complementary, class of insertion sites. We show that donor-doping of anatase TiO_2 to form large numbers of cationic vacancies allows the complementary insertion of Li^+ and Mg^{2+} in a dual-ion cell with a net increase in cell energy density, due to a combination of an increased reversible capacity, an increased operating voltage, and a reduced polarization. By tuning the lithium concentration in the electrolyte, we achieve full utilization of the Ti^{4+}/Ti^{3+} redox couple with excellent cyclability and rate capability. We conclude that native interstitial sites preferentially accommodate Li^+ ions, while Mg^{2+} ions occupy single-vacancy sites. We also predict a narrow range of electrochemical conditions where adjacent vacancy pairs preferentially accommodate one ion of each species, *i.e.*, a $[Li_{Ti}+Mg_{Ti}]$ configuration. These results demonstrate the implementation of additional host sites such as cationic sites as an effective approach to increase the energy density in dual-ion batteries.

Introduction

Lithium-ion batteries find use in diverse applications, including portable electronic devices, electric vehicles and large-scale energy-storage systems.[1] With the growing demand for energy, development of post-lithium-ion batteries with superior performance is critical. In this

context, magnesium secondary batteries that use a Mg metal anode and an intercalation-type cathode are attractive candidates.[2] Mg metal anodes have a large volumetric capacity (3832 mA h cm^{-3}), are resistant towards dendrite formation,[3,4] and are stable against air and moisture exposure, giving higher theoretical energy densities and improved safety relative to conventional lithium-ion batteries.

Despite these appealing properties, the development of rechargeable Mg batteries faces many challenges.[5] The higher formal charge of Mg^{2+} ions implies strong interactions with the anion sub-lattice in an intercalation host material, causing slow solid-state Mg^{2+} diffusion compared with Li^+ analogues.[5] Several strategies have been proposed to improve solid-state Mg^{2+} diffusion, including using electrodes that contain "soft" polarizable anions[6,7] or operating cells at high temperatures,[8] identifying host frameworks with low potential-energy barriers to Mg^{2+} diffusion,[9–11] and more recently, exploiting dual-ion intercalation chemistries.[12–14] In the context of this latter approach, we focus on "dual Mg/Li-ion" batteries, where the electrochemical cell consists of a Mg metal anode, an intercalation compound cathode, and a hybrid electrolyte that contains both Mg^{2+} and Li^+ ions as charge carriers. The concentration of Li^+ in the hybrid electrolyte dictates the insertion chemistry, which can vary from pure Mg^{2+} intercalation (when no Li^+ is present in the electrolyte), mixed Mg^{2+}/Li^+ intercalation (for low Li^+ electrolyte concentrations), to pure Li^+ intercalation (for high Li^+ electrolyte concentrations).[12] One particularly interesting characteristic of using a hybrid dual-salt electrolyte is that co-intercalation of Li^+ and Mg^{2+} into a host electrode can give enhanced Mg^{2+} diffusion rates, which has been attributed to interactions between the co-inserted Li^+ and Mg^{2+} ions lowering the activation energy for Mg^{2+} diffusion.[15] Although this enhanced kinetics relative to single-ion Mg^{2+} cells makes dual-ion batteries an exciting prospect, they

remain at an early stage of development, and only a small number of cathode materials are known that can simultaneously intercalate both Li^+ and Mg^{2+}.

In a typical intercalated compound, the atomic structure possesses vacant sites that can accommodate cations. Anatase TiO_2 is a well-known example of intercalation compound that can accommodate Li^+ or Na^+ ions. Its interstitial sites, however, appear to be inactive towards Mg^{2+} insertion. Nonetheless, anatase TiO_2 can be chemically modified to introduce a high concentration of titanium vacancies, which can accommodate Mg^{2+} ions.[16] From a purely thermodynamic perspective, the calculated intercalation energies at titanium vacancy sites, with respect to Mg and Li-metal, are -3.3 eV for Mg^{2+} and -2.7 eV for Li^+. These favorable energies suggest the possibility of simultaneous intercalation of Mg^{2+} and Li^+ ions in a cation-deficient material, giving an increased energy-density. For the purposes of developing electrode materials for dual-ion batteries, we then propose the use of a host framework that features different types of host sites (interstitial and titanium vacancies) that can co-intercalate two different charge-carrier species, giving a net increase in energy density. Here, we report the success of this strategy, where using a hybrid Li^+/Mg^{2+} electrolyte with a cation-deficient TiO_2 electrode gives a capacity of close to 300 mA h g^{-1}, providing a two-fold increase in capacity, a reduced polarizability, and a 0.5 V voltage increase compared with a pure Mg electrolyte. This study provides a proof-of-concept for a new design strategy for dual-ion batteries and gives a further example of application of defect chemistry for engineering high-energy density batteries.

Results and discussion

To investigate the role of cationic vacancies in dual-ion insertion chemistry, we consider two types of anatase TiO_2: a defect-free compound with formal stoichiometry of TiO_2, and a highly defective anatase with the chemical composition $Ti_{0.78}\square_{0.22}O_{1.12}F_{0.40}(OH)_{0.48}$,[17] where

□ refers to a titanium vacancy. The chemical composition was determined using ^{19}F solid-state NMR to assess the fluorine content and structural analysis based on PDF data to quantify the number of Ti vacancies, with the number of OH groups then inferred from the constraint of net electroneutrality considering the general chemical formula $Ti_{1-x-y}\square_{x+y}O_{2-4(x+y)}F_{4x}(OH)_{4y}$ with titanium and oxide ions oxidation states being +IV and –II, respectively.[17]

The electrochemical properties were investigated using Mg as the anode and the all-phenyl complex (APC) $Mg_2Cl_3^+AlPh_2Cl_2^-$ in tetrahydrofuran (THF) as the electrolyte. LiCl was selected as lithium source because it does not alter the electrochemical stability of the electrolyte or the deposition/dissolution of magnesium **(Figure S1)**.[13,18] The concentration was varied from 0 M to 1 M, with the upper value being the solubility limit of LiCl in THF. Note, that salts such as $LiBH_4$ with higher solubility can be envisioned to increase the cell energy density.[18] **Figure 1** presents the galvanostatic discharge–charge curves and the corresponding derivatives curves obtained for both anatase samples, using a three-electrode Swagelok cell. With no lithium in the electrolyte, anatase TiO_2 shows a poor ability to accommodate Mg, with a reversible capacity of only ~25 mA h g^{-1} in a Mg cell.[16] Introducing lithium into the electrolyte enhances the electrochemical activity of pure anatase TiO_2 **(Figure 1a)**. The addition of a small amounts of lithium significantly improves the reversible capacity, which reaches a threshold between 0.2 M and 1 M of LiCl with a reversible capacity of ca. 200 mA h g^{-1}. Moreover, upon introducing lithium, we observe the appearance of a plateau region characteristic of a phase transition from tetragonal anatase to the orthorhombic lithium titanate[19], highlighting the contribution of Li^+ ions in the charge storage mechanism. The voltage of the plateau progressively rises (upon discharge) with increasing lithium concentration **(Figure 1b)**. At 1.0 M of LiCl, the plateau

region occurs at a voltage of 0.93 V *vs*. Mg^{2+}/Mg or 1.67 V *vs*. Li^{+}/Li, which is close to that observed in a lithium cell.[19]

In $Ti_{0.78}\square_{0.22}O_{1.12}F_{0.40}(OH)_{0.48}$, the presence of large numbers of Ti vacancies enables magnesium intercalation (without Li in the electrolyte) with a reversible capacity of 150 mA h g^{-1} (*vs*. 25 mA h g^{-1} for TiO_2),[16] albeit with a high polarization, as shown in **Figure 1c**. For this defect-rich electrode, adding lithium to the electrolyte improves the reversible capacity and, reduces polarization, thus significantly increases the cell energy density. These two effects are observed even for low concentrations of lithium (0.05 M–0.1 M) with the capacity reaching more than 250 mA h g^{-1} at 0.1 M. For 1.0 M of LiCl, we measure a capacity of 300 mA h g^{-1} (*vs*. 200 mA h g^{-1} for TiO_2). Lithium and magnesium insertion into anatase were previously shown to imply the Ti^{4+}/Ti^{3+} redox couple.[20,16] The theoretical maximum capacity based on the Ti^{4+}/Ti^{3+} redox couple is 290 mA h g^{-1} showing a full utilization of the active centers. This capacity is, to our knowledge, the highest reported for a dual-ion battery and demonstrates the potential benefits of using defect-engineered-electrodes in these devices. In addition, as observed on the derivative curves **(Figure 1d)**, the insertion voltage progressively increases with the lithium concentration, with peaks shifting from 0.77 V for 0.05 M LiCl to 1 V for 1.0 M LiCl.

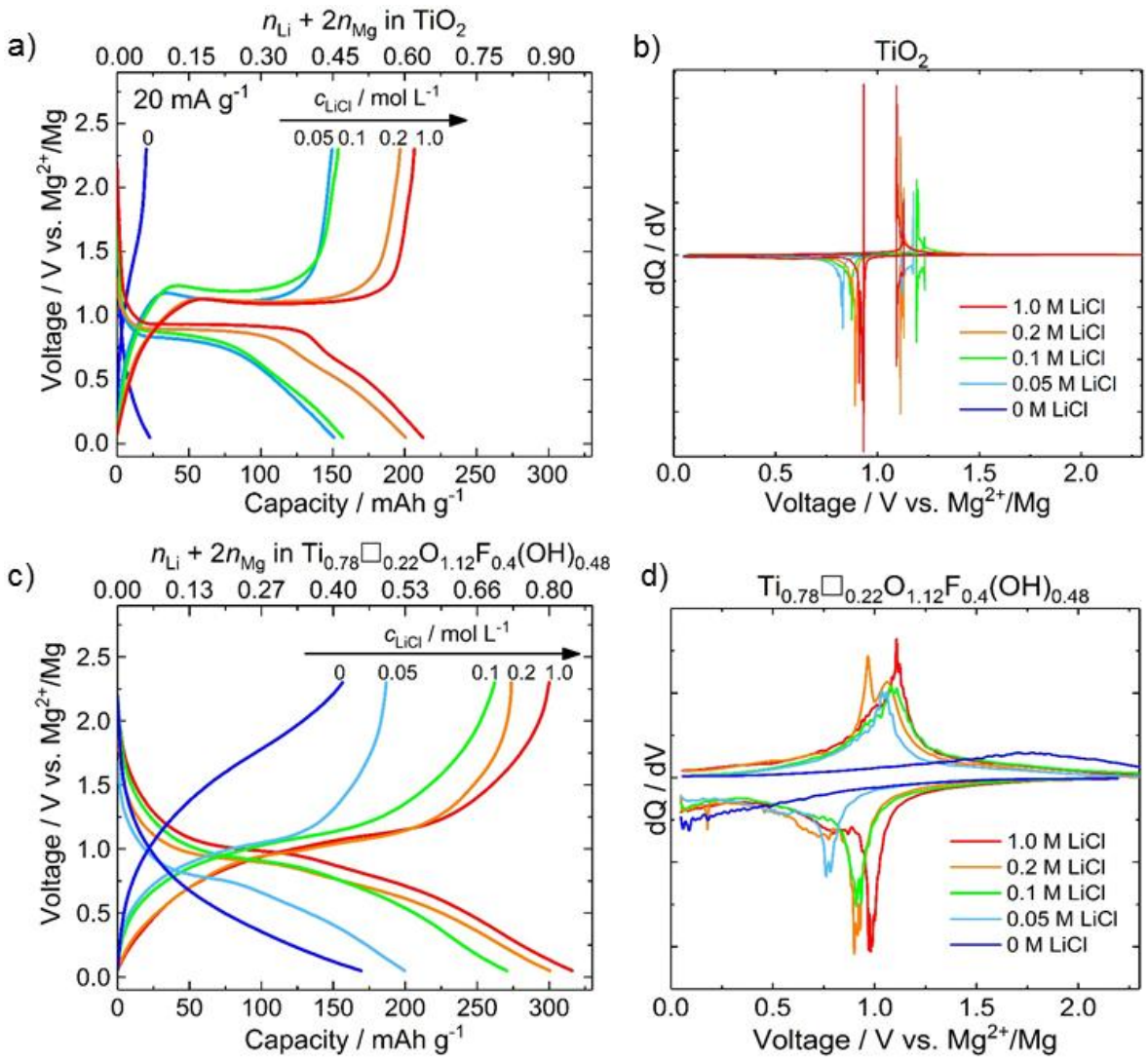

Figure 1. Discharge–charge curves and corresponding derivative curves for Mg/TiO_2 **(a,b)** and Mg/$Ti_{0.78}\square_{0.22}O_{1.12}F_{0.40}(OH)_{0.48}$ **(c,d)** cells cycled at 20 mA g^{-1} using 0.2 M APC with various LiCl concentrations. The discharge-charge curves were obtained after two cycles of activation.

We now consider the rate capability of $Ti_{0.78}\square_{0.22}O_{1.12}F_{0.40}(OH)_{0.48}$ as a function of the lithium concentration in the electrolyte. **Figure 2a** shows the evolution of the capacity when increasing the current density, for different lithium-electrolyte concentrations. When increasing the lithium concentration, a significant improvement in the reversible capacity under increasing *C*-rate is observed. At current densities below 100 mA g^{-1}, high reversible capacities of 260 and

275 mA h g^{-1} are obtained for 0.2 M and 1 M of LiCl, respectively. At current densities higher than 100 mA g^{-1}, the rate capability depends on the lithium concentration High capacities, up to 200 mA h g^{-1} under 1000 mA g^{-1}, were obtained for a lithium concentration of 1 M. These capacities are more than 2 times higher than those obtained for stoichiometric TiO_2 under the same conditions (**Figure S2**). Subsequently, we cycled cells containing electrolytes with 0.2 M and 1 M LiCl under 1000 mA g^{-1} for 400 cycles **(Figure 2b)**. While the capacity largely depends on the lithium concentration, in both cases, the cell shows excellent cyclability, with capacity retention greater than 90 % after 400 cycles.

To better understand the lithium concentration dependence on the electrochemical properties, the proportions of Li^+ and Mg^{2+} ions within discharged electrodes were assessed using inductively coupled plasma atomic emission spectroscopy (ICP-AES). **Figure 2c** gathers the Li, Mg content, with respect to chemical formulae, measured after discharging electrodes under different electrolytic conditions. In pure APC (no LiCl), the number of Mg^{2+} matches the measured discharge capacity for both anatase samples. The introduction of 0.2 M LiCl produces a significant increase in the capacity, which is almost entirely due to the additional insertion of lithium. Strikingly, we observed that anatase TiO_2 can accommodate twice as much Mg^{2+} after the introduction of lithium in the electrolyte (although this remains a small contribution relative to the Li^+ insertion). This confirms the work of Ichitsubo *et al.*[15] who have proposed that interactions between intercalated Li^+ and Mg^{2+} increase the ability of the framework to accommodate Mg^{2+} ions. In the case of $Ti_{0.78}\square_{0.22}O_{1.12}F_{0.40}(OH)_{0.48}$, our analysis confirms the co-intercalation mechanism, with 0.47 Li^+ and 0.18 Mg^{2+} ions (0.83 electron) inserted per 0.78 mole of Ti, which is slightly higher than theoretically expected based on Ti^{4+}/Ti^{3+} redox couple. Such a difference can be explained by extra-capacity arising from the degradation of the

electrolyte[21] which is common for this type of materials. At 1.0 M of LiCl, the proportion of lithium inserted into anatase increases significantly, showing that the intercalation chemistry becomes dominated by this ion. Moreover, under increasing current densities, the proportion of inserted Li^+ increases with respect to Mg^{2+}, which may be due to a higher solid-state diffusion rate of Li^+ in $Ti_{0.78}\square_{0.22}O_{1.12}F_{0.40}(OH)_{0.48}$.

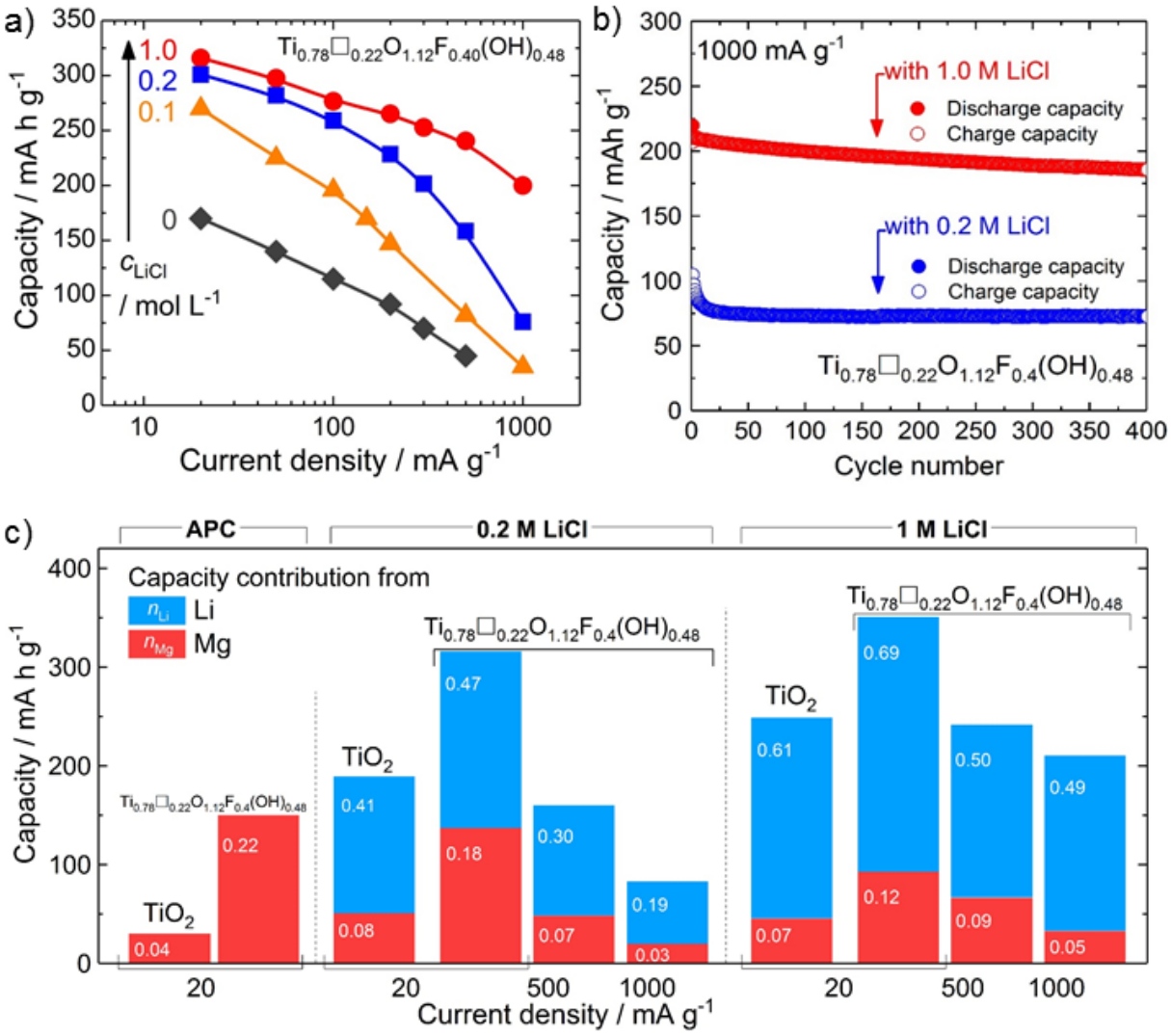

Figure 2. a) Rate capability plots of Mg/$Ti_{0.78}\square_{0.22}O_{1.12}F_{0.40}(OH)_{0.48}$ cells cycled with different lithium concentrations. **b)** Long term cycling of Mg/$Ti_{0.78}\square_{0.22}O_{1.12}F_{0.40}(OH)_{0.48}$ cells under 1000 mA g^{-1} with 0.2 M and 1.0 M LiCl. **c)** Li and Mg contents in discharged electrodes of anatase

TiO_2 and $Ti_{0.78}\square_{0.22}O_{1.12}F_{0.40}(OH)_{0.48}$ using different electrolytes, from chemical analyses (ICP-AES).

To further investigate the intercalation mechanism of dual-ions in $Ti_{0.78}\square_{0.22}O_{1.12}F_{0.40}(OH)_{0.48}$, we focused on the hybrid electrolyte with 0.2 M APC and 0.2 M LiCl, giving 2 Mg^{2+} per 1 Li^+. Galvanostatic-intermittent-titration-technique (GITT) was applied during the first discharge **(Figure 3a)**.[22] The absence of a constant voltage plateau is consistent with a co-intercalation mechanism occurring via a solid-solution behavior, in contrast with the phase transformation mechanism[19] observed for stoichiometric TiO_2. This solid solution behavior was previously observed for pure Li^+ and Mg^{2+} intercalation chemistries in $Ti_{0.78}\square_{0.22}O_{1.12}F_{0.40}(OH)_{0.48}$ and was attributed to the presence of cationic vacancies and heterogeneous anion environments, that suppress the formation of pairs of edge-sharing LiO_6 octahedra associated with the tetragonal to orthorhombic phase transition in pure TiO_2.[16,17,23,24] Moreover, GITT allows the equilibrium potential to be determined at different states of discharge. The difference between the measured potential and the equilibrium potential represents the overpotential (η), which includes contributions from charge- and mass-transfer kinetics, and other chemical events.[22] Although the physical origin of the rate-determining step in the overpotential cannot be simply identified,[25] we have compared the overpotential measured with and without lithium in the electrolyte **(Figure 3a)**. The intercalation of Mg^{2+} within $Ti_{0.78}\square_{0.22}O_{1.12}F_{0.40}(OH)_{0.48}$ induces a progressive increase of the overpotential, which may be related to the concentration dependence of the solid-state diffusion of Mg^{2+}within the anatase framework.[16,26] On the other hand, the presence of lithium induces a noticeable

decrease of the overpotential even though the total number of inserted ions is far greater using the hybrid electrolyte.

To further understand the dual-ion intercalation mechanism, the number of ions inserted during the first discharge was assessed by ICP-AES **(Figure 3b)**. This revealed that co-intercalation of Li^+ and Mg^{2+} occurs simultaneously during the whole discharge process. Such a behavior is in contrast with the Mg-Li dual ion insertion mechanism studied by Ichitsubo et *al*.[15] who observed that Mg insertion occurs after the preferential intercalation of Li^+ ions within Mo_6S_8 host structure. At the end of the reduction, the inserted Mg^{2+} stoichiometry is 0.18, which is lower than in the case of pure APC electrolyte. In the latter case, Mg^{2+} ions are selectively inserted and fully occupy the titanium vacancies, giving a final Mg stoichiometry of 0.22.[16] We suggest that such a difference might be due to a small fraction of Li^+ (0.04 Li^+) being inserted within the titanium vacancy sites as further confirmed by DFT-calculations (see below). To probe the structural changes induced by the dual-ion intercalation, we used the pair distribution function (PDF) obtained by Fourier Transform of the total-scattering structure factors.[27] The PDF represents the probability of finding a pair of atoms separated by a distance *r*, and is particularly well suited to probe the structure of disordered material.[28] The discharge reaction produces a broadening of the PDF peaks, which suggests overall reduced long-ranged ordering in the structure **(Figure 3c)**. Assuming a solid-solution mechanism, as indicated by the GITT data described above, the PDF of the discharged electrode was fitted using the pristine tetragonal symmetry. The refinement confirms that the long-ranged anatase structure is maintained and further points to local structural distortions as revealed by the occurrence of features in the difference curve that cannot be captured by the used structural model. These structural distortions might be due to a difference in terms of polarizing power of the two charge

carriers, resulting in different local cation–anion bond lengths and local disruption to the framework periodicity. The dual-ion intercalation is also characterized by changes in the unit cell parameters: $a = 3.7991(7)$ Å, $c = 9.475(2)$ Å for the pristine electrode, while $a = 3.875(2)$ Å, $c = 9.325(6)$ Å for the discharged sample. Previous works have shown that for intercalation of Mg^{2+} ions in titanium vacancies, using pure APC as electrolyte, the unit cell parameters do not vary ($\Delta V/V \sim 0.6\%$).[16] Furthermore, in a pure lithium-ion cell, lithium insertion into anatase $Ti_{0.78}\square_{0.22}O_{1.12}F_{0.40}(OH)_{0.48}$ modifies the unit cell parameters in proportion with the lithium concentration (Vegard's law) with a increase and c decrease. We therefore conclude that the changes in the unit cell parameters observed for dual-ion intercalation are due to the insertion of lithium within the native interstitial sites (4b Wyckoff site). According to the unit cell parameter values, it is possible to assess a concentration of lithium located at interstitial sites leading to 0.30–0.35 Li^+.[17,29,30] We further attempted to refine the presence of Mg^{2+} within the interstitial sites which led to negligible value. Finally, we have confirmed the selective insertion of Mg^{2+} at the Ti vacancy site (4a Wyckoff site) by refining its rate occupancy. Based on chemical and PDF analyses, we hypothesize that the insertion mechanism occurs as follows:

$$[Ti_{0.78}\square_{0.22}]^{4a}O_{1.12}F_{0.40}(OH)_{0.48} + (x+y)\,Li^+ + z\,Mg^{2+} + (x + y + 2z)\,e^-$$

$$\rightleftarrows [Li_x]^{4b}[Li_yMg_zTi_{0.78}\square_{0.22-(y+z)}]^{4a}O_{1.12}F_{0.40}(OH)_{0.48}.$$

With 4a and 4b being the Wyckoff sites of titanium and interstitial sites, respectively; $x \approx 0.3$–0.35, $y \approx 0.04$ and $z \approx 0.18$, leading to a capacity of 264 mA h g^{-1}–284 mA h g^{-1}, which is close to that measured experimentally, a small fraction of this capacity being assigned to electrolyte decomposition. During the charge, the structure of the pristine electrode is fully recovered ($a = 3.805(1)$ Å, $c = 9.477(3)$ Å) demonstrating the reversible co-insertion of Li^+ and Mg^{2+}.

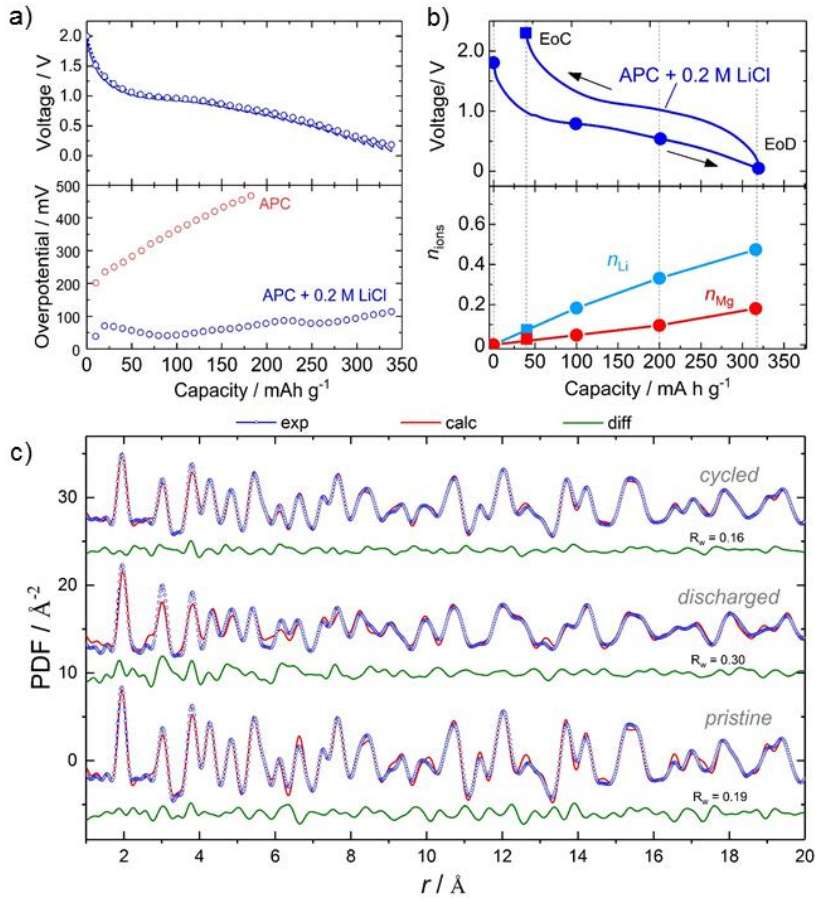

Figure 3. a) Galvanostatic-intermittent-titration-technique performed during the first discharge (bottom) and evolution of the overpotential during the first discharge with (APC +0.2M of LiCl) and without (APC) lithium. **b)** Chemical analyses (ICP-AES) of Li, Mg contents during the first cycle. The electrolyte was APC with 0.2M of LiCl. **c)** Refinements of the PDF data of pristine, discharged and cycled electrodes.

^{19}F solid-state NMR was previously shown to be a suitable marker for the presence of different cationic species in the vicinity of fluorine atoms.[16,17,24] **Figure 4** shows the ^{19}F MAS NMR spectra of the pristine, discharged, and charged electrodes using hybrid electrolyte 0.2 M APC + 0.2 M LiCl and 1 M LiCl (fits are given as Supporting Information, **Figures S3−S6** and **Tables S1−S4**). In the pristine compound, the environments F-Ti^{IV}_3, F-$Ti^{IV}_2\square$ and F-$Ti^{IV}\square_2$ are characterized by distinct chemical shift values ranging from -88 ppm to 98 ppm.[17] The

intercalation of Li^+/Mg^{2+} ion being simultaneous with the reduction of Ti^{4+} ions into Ti^{3+} ions, the number of potential fluorine environments dramatically increases from the pristine compound to the discharged and charged electrodes in which the cationic site is occupied by four different cations (Ti^{4+}, Ti^{3+}, Li^+ and Mg^{2+}) or remaining vacancies, without forgetting the additional environments resulting from Li^+ ions located at interstitial sites. Based on the ^{19}F NMR chemical shift values of the environments $Ti^{IV}\square_2$-F, $Ti^{IV}_2\square$-F and Ti^{IV}_3-F in $Ti_{0.78}\square_{0.22}O_{1.12}F_{0.40}(OH)_{0.48}$, F-$Ti^{III}_2$-F in TiF_3 (-145 ppm[16]), F-Mg_3 in MgF_2 (-197 ppm[31]) and F-Li_6 in LiF (-204 ppm[31]), and on the decrease of the ^{19}F chemical shift value when the coordination number of fluorine increases, the intercalation of Li^+ and/or Mg^{2+} ions in titanium vacancies and the reduction of a Ti^{4+} ion into a Ti^{3+} ion induce a decrease of the ^{19}F chemical shift value of the neighbouring ^{19}F nucleus. And indeed, after Li^+/Mg^{2+} co-intercalation, as after intercalation of Mg^{2+}[16] or Li^+,[32] we observed an overall offset of chemical shift toward lower values. The weighted average chemical shift value ($<^{19}F\ \delta_{iso}>$) decreases from 25 ppm for the pristine sample to -150 ppm for the discharged electrode using hybrid electrolyte 0.2 M APC + 1 M LiCl (**Tables S1−S4**). This shift is concomitant with the disappearance of the resonance characteristic of the F-$Ti^{IV}\square_2$ species and the decrease (down to zero for the discharged electrode using hybrid electrolyte 0.2 M APC + 1 M LiCl) of the relative intensity of the resonance characteristic of the F-$Ti^{IV}_2\square$ species, indicating the insertion of Li^+ and Mg^{2+} in the Ti vacancies (and/or the reduction of Ti^{IV} in Ti^{III}). The co-intercalation reaction is also accompanied by the appearance of sharp resonances centered at around -200 ppm, lying within the δ_{iso} values of F-Mg_3 and F-Li_6 environments in MgF_2 and LiF, respectively.[31] Upon charging, the relative intensity of these resonances decreases while new ones appears at about –180 ppm. Concomitantly, the relative intensity of the resonances at about 0 ppm increases and

overall, the weighted average chemical shift value increases, in agreement with a partial deintercalation process.

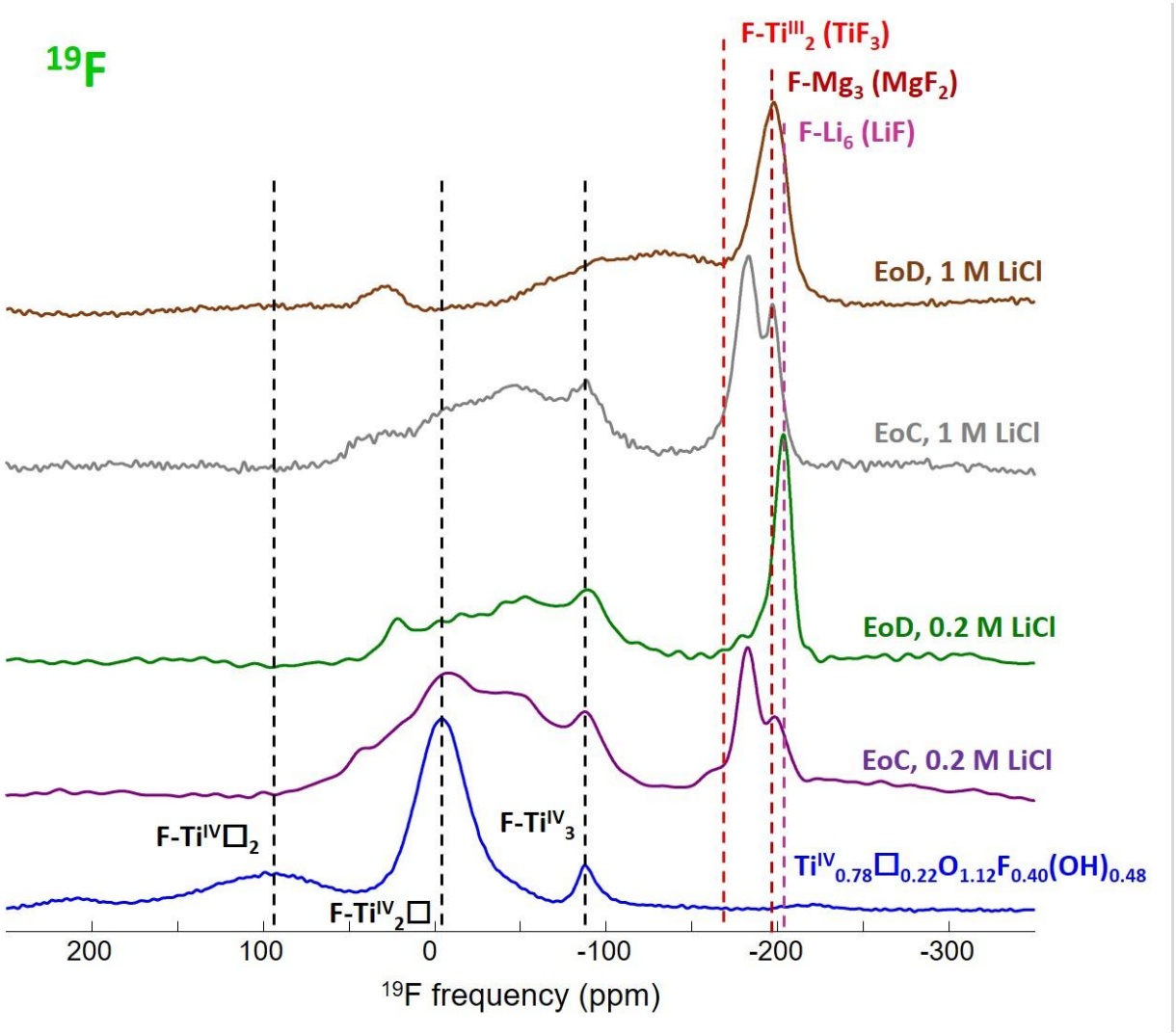

Figure 4. ^{19}F solid-state MAS NMR spectra of pristine (60 kHz) and electrochemically discharged (EoD) and charged (EoC) electrodes (64 kHz) using hybrid electrolyte 0.2 M APC + 0.2 M LiCl and 1 M LiCl. The black dashed lines indicate the ^{19}F δ_{iso} values of F-Ti^{IV}_3, F-$Ti^{IV}_2\square$ and F-$Ti^{IV}\square_2$ environments in $Ti_{0.78}\square_{0.22}O_{1.12}F_{0.40}(OH)_{0.48}$.[16,17] The red, brown and mauve dashed lines refer to the ^{19}F δ_{iso} values of the F-Ti^{III}_2-F environment in TiF_3,[16] F-Mg_3 in MgF_2[31] and F-Li_6 environment in LiF,[31] respectively.

^{7}Li solid state MAS NMR spectra of the electrochemically prepared samples were also recorded (**Figure S7**). The integrated intensity of the signal decreases upon charging (**Figure 5**) confirming the deintercalation of lithium, *i.e.*, the reversibility of the reaction. Whereas paramagnetic compounds exhibit lithium resonances shifted over a range of several hundred ppm,[33] due to the Fermi contact interaction, despite containing $3d^1$ titanium(III), the electrochemically discharged and charged electrodes, as lithiated anatase,[34–36] and chemically lithiated $Ti_{0.78}\square_{0.22}O_{1.12}F_{0.40}(OH)_{0.48}$,[32] show ^{7}Li NMR resonances inside the normal diamagnetic ^{7}Li shift range (ca. 5 to −5 ppm).[37] Wagemaker et al.[35] concluded that conduction, rather than paramagnetism, is the dominant interaction in anatase. Distributions of quadrupole interactions and chemical shifts due to disordered environments and interactions with electrons in the conduction band then account for the line broadening and the intense spinning sidebands. Spectral decompositions of the slightly asymmetric central lines require two contributions (as an example, the fit of one the spectrum is given as SI (**Figure S8**)). For chemically lithiated $Ti_{0.78}\square_{0.22}O_{1.12}F_{0.40}(OH)_{0.48}$ samples, as the Li rate increases, the ^{7}Li signal broadens and shifts slightly in a positive direction and the intensity of the spinning sidebands increases. Such trends are only partially fulfilled for the four electrochemically discharged and charged electrodes: the larger weighted average chemical shift value and stronger spinning sidebands are observed for the higher Li rate (**Table S5**).

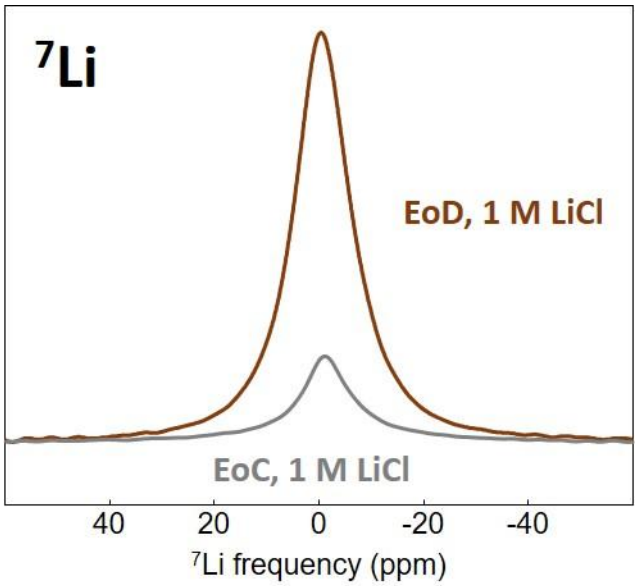

Figure 5. Expansions of the central lines of the non-normalized ^{7}Li MAS (44 kHz) NMR spectra of the electrochemically discharged (EoD) and charged (EoC) electrodes using hybrid electrolyte 0.2 M APC + 1 M LiCl.

To better understand the competitive insertion of Li^{+} and Mg^{2+} into these materials, and the effect of the electrolyte lithium concentration, we performed a series of density functional theory (DFT) calculations of Li^{+} and Mg^{2+} insertion in three models: (i) at an interstitial site in stoichiometric anatase TiO_2, (ii) at a single titanium vacancy site in F-doped TiO_2, and (iii) at a double vacancy pair of sites in F-doped TiO_2.

Computational studies of intercalation energies usually present these with respect to the corresponding reference phase (metallic Li or Mg). Dividing by the formal charge of the ion gives the corresponding insertion voltage with respect to this metallic reference electrode.**[38]** For a dual-ion electrode, the intercalation thermodynamics depends on the electrochemical potentials of both ions. With metallic Mg as the reference electrode, the Mg^{2+} electrochemical potential at equilibrium is one half of the (open circuit) cell voltage. The electrochemical

potential of Li^+, however, is not as simply defined, but is assumed to vary approximately as $\Delta\tilde{\boldsymbol{\mu}}_{\mathbf{Li}} = \tilde{\boldsymbol{\mu}}^{\mathbf{0}}_{\mathbf{Li}} + \boldsymbol{qV}$, where $\tilde{\boldsymbol{\mu}}^{\mathbf{0}}_{\mathbf{Li}}$ is the Li electrochemical potential at zero voltage, $q = 1$, and V is the applied voltage with respect to the metallic Mg electrode. In general, $\tilde{\boldsymbol{\mu}}^{\mathbf{0}}_{\mathbf{Li}}$ is unknown, but is assumed to increase with the concentration of Li in the electrolyte, and in principle can be calculated if the activity of Li^+ in the electrolyte is known. For our analysis, we consider $\Delta\tilde{\boldsymbol{\mu}}_{\mathbf{Li}}$ and $\Delta\tilde{\boldsymbol{\mu}}_{\mathbf{Mg}}$ as free parameters and calculate the thermodynamically favored intercalation product as a function of both electrochemical potentials (**Figure 6**).

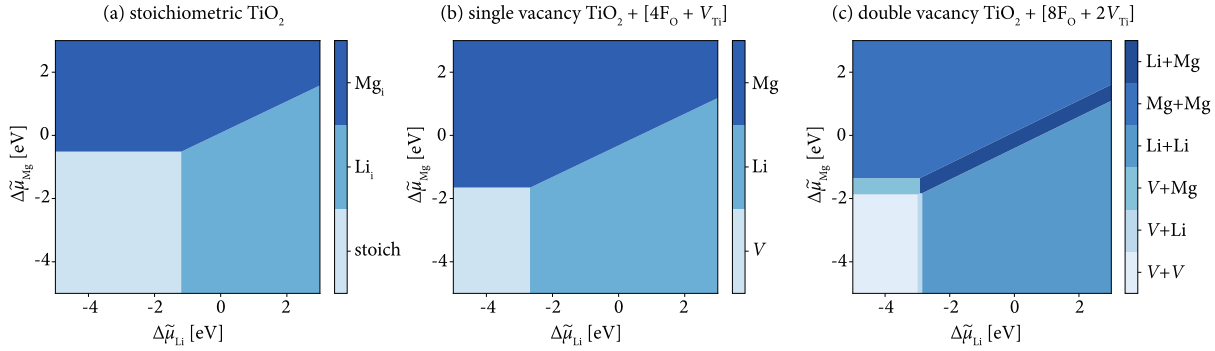

Figure 6. The lowest energy intercalation products at a paired V_{Ti}+V_{Ti} site, as a function of magnesium and lithium electrochemical potentials relative to the elemental metals; $\Delta\mu_{Mg}$ and $\Delta\mu_{Li}$), calculated from DFT data. *Source*: source data, figure files, and plotting scripts are available under the CC-BY-4.0 license as part of reference [39].

For insertion at an interstitial site in stoichiometric anatase TiO_2 (**Figure 6a**) we predict simple behavior. If both $\Delta\tilde{\boldsymbol{\mu}}_{\mathbf{Li}}$ and $\Delta\tilde{\boldsymbol{\mu}}_{\mathbf{Mg}}$ are low, neither cation is thermodynamically predicted to intercalate. Increasing either $\Delta\tilde{\boldsymbol{\mu}}_{\mathbf{Li}}$ or $\Delta\tilde{\boldsymbol{\mu}}_{\mathbf{Mg}}$ while keeping the other chemical potential low, we predict Li intercalates at $\Delta\tilde{\boldsymbol{\mu}}_{\mathbf{Li}} > -1.19$ eV, and Mg intercalates at $\Delta\tilde{\boldsymbol{\mu}}_{\mathbf{Mg}} > -0.51$ eV (+0.25 V with respect to the Mg electrode). If both $\Delta\tilde{\boldsymbol{\mu}}_{\mathbf{Li}}$ and $\Delta\tilde{\boldsymbol{\mu}}_{\mathbf{Mg}}$ are high, intercalation is competitive and the preferentially inserted cation depends on their relative electrochemical potentials. For insertion at a single [V_{Ti} + 4F_O] vacancy in F-doped anatase TiO_2 (**Fig. 6b**), the behavior is qualitatively

similar to stoichiometric anatase, but both cations intercalate at lower chemical potentials. Li^+ intercalates at $\Delta\tilde{\mu}_{Li} > -2.67$ eV and Mg^{2+} intercalated at $\Delta\tilde{\mu}_{Mg} > -1.65$ eV; again, competitive insertion of either Li^+ or Mg^{2+} occurs when both electrochemical potentials are high. For the double vacancy model, the thermodynamically predicted behavior is broadly similar to the single vacancy, but becomes more complex because there are now two vacant sites that can potentially accommodate either Li^+ or Mg^{2+} (**Fig. 6c**). As is the case for the stoichiometric and single-vacancy models, at low $\Delta\tilde{\mu}_{Li}$ and low $\Delta\tilde{\mu}_{Mg}$ neither cation intercalates. With increasing $\Delta\tilde{\mu}_{Li}$ (low $\Delta\tilde{\mu}_{Mg}$), we find a narrow chemical potential range where one Li^+ is inserted and the second insertion site is empty. For $\Delta\tilde{\mu}_{Li} > -2.85$ eV, Li^+ is inserted at both sites. With increasing $\Delta\tilde{\mu}_{Mg}$ (low $\Delta\tilde{\mu}_{Li}$), we again find a narrow chemical potential range where one Mg^+ is inserted and the second insertion site is empty, and for $\Delta\tilde{\mu}_{Mg} > -1.36$ eV Mg^{2+} is inserted at both sites. When both $\Delta\tilde{\mu}_{Li}$ and $\Delta\tilde{\mu}_{Mg}$ are high ($\Delta\tilde{\mu}_{Li} > -2.92$ eV, $\Delta\tilde{\mu}_{Mg} > -1.83$ eV), we also find a range of chemical potentials where mixed insertion of [Li^+ + Mg^{2+}] is thermodynamically favored. The predicted staged insertion of first one cation and then a second, and the predicted mixed insertion of both Li^+ and Mg^{2+} within certain chemical potential ranges are both due to the second insertion energy of Li^+ and Mg^{2+} being less favorable than the first, with this effect stronger for Mg^{2+}. This behavior is due to structural distortions induced by the first cation insertion, which then makes the second insertion less favorable. This effect is illustrated in **Fig. 7** for Mg^{2+} insertion, which shows the distances between pairs of anions at opposite vertices of each V_{Ti} octahedron and how these change as either Li^+ or Mg^{2+} are sequentially inserted. Before cation insertion, the V_{Ti} sites are tetragonally distorted octahedra with equatorial anion–anion distances of ~3.9 Å and an axial anion–anion distance of ~4.6 Å **(Fig. 7a)**. Insertion of one Li^+ or one Mg^{2+} causes a reduction of this tetragonal distortion at the insertion site, with Mg^{2+}-insertion having a stronger effect,

reflecting a preference for Mg^{2+} to adopt octahedral coordination (**Figs. 7b and 7c**). For both Li^{+} and Mg^{2+}, the reduced tetragonal distortion at the first insertion site is accompanied by an increased distortion of the neighboring still-vacant site. Inserting a second cation at the second V_{Ti} site now carries an additional energy cost, because this vacant site is geometrically more dissimilar from the optimal geometry for an occupied site. This asymmetric energy cost between first and second cation insertions is more distinct for Mg^{2+} than for Li^{+} because Mg^{2+} has a stronger preference for regular octahedral coordination, and induces a larger change in the host lattice structure upon the first insertion.

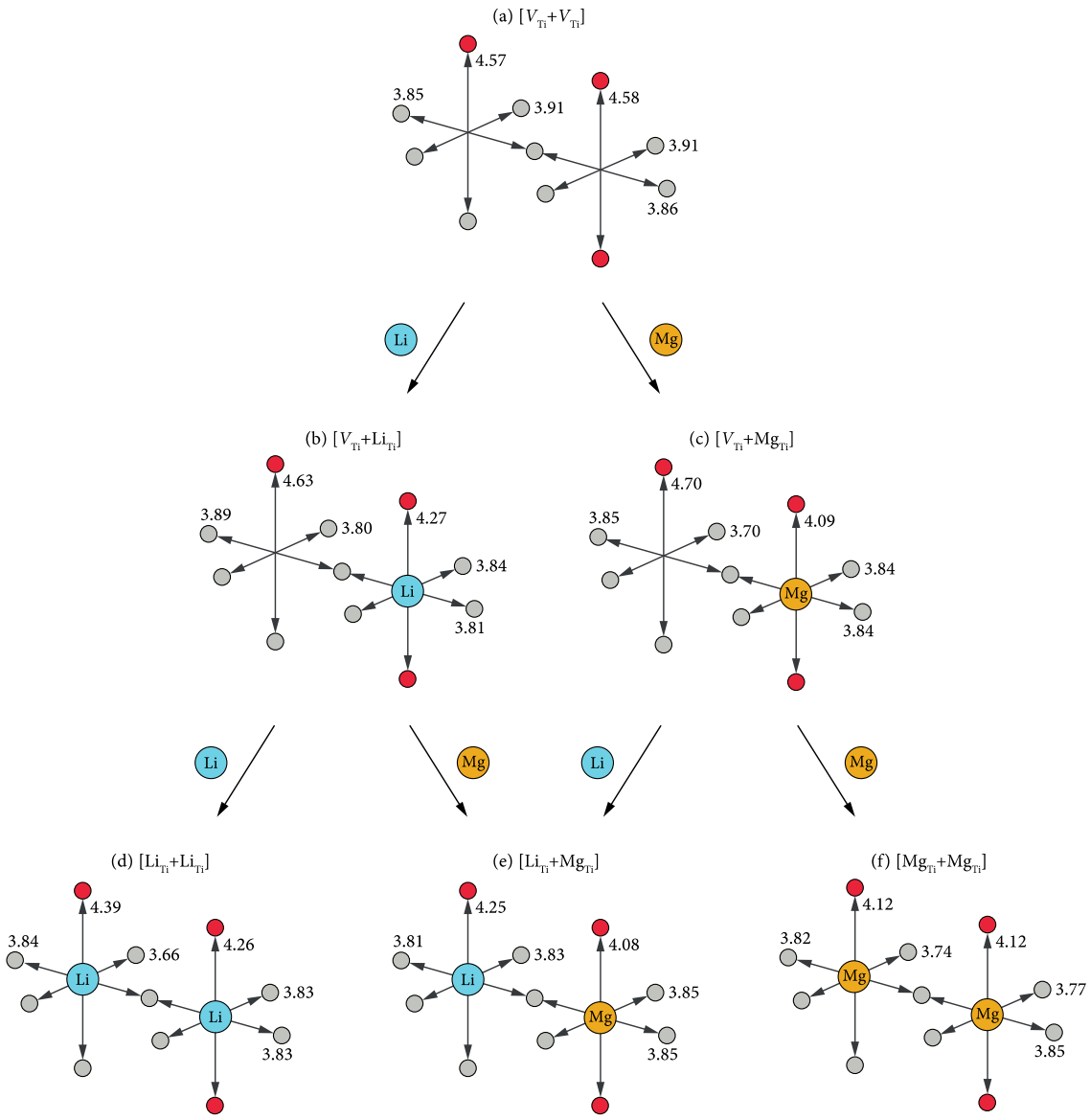

Figure 7. Changes in geometry of the V_{Ti} octahedra in the [V_{Ti}+V_{Ti}] paired-vacancy model for different combinations of Li^+ and Mg^{2+} insertion. The relevant DFT-optimised structure files are available under the CC-BY-4.0 license as part of reference [39].

This computational analysis provides an explanation for the competitive Li^+/Mg^{2+} dual-ion insertion we observe in our experiments, and how the contribution from Li^+ and Mg^{2+} depends on the concentration of lithium ions in the electrolyte. Moreover, the ion insertion behavior is predicted to depend on the type of sites involved. Our calculations predict a broad range of

electrochemical conditions under which interstitial sites preferentially accommodate Li^+ ions and vacant cation sites preferentially accommodate Mg^{2+} ions. In our experiments, we suggest that this co-intercalation of Li^+ and Mg^{2+} is achieved for an electrolyte composition of 0.2 APC and 0.2 M LiCl, *i.e.*, 2 Mg^{2+} per 1 Li^+, with lithium preferentially inserted in the interstitial sites and magnesium ions inserted at the singly-vacant sites. By comparing the number of titanium vacancy sites and inserted Mg^{2+} ions, we suggest that some Li^+ ions are inserted in the double-vacancy forming [Li_{Ti}+Mg_{Ti}], as predicted within a narrow range of thermodynamic conditions by our DFT results. As the lithium concentration increases, we predict preferential dual insertion of Li at paired vacancies to form [Li_{Ti}+Li_{Ti}], in agreement with the change in proportion of inserted Li vs. Mg we observe experimentally.

Conclusion

We have investigated the effect of chemically introducing cationic vacancies into an anatase TiO_2 host structure for use as a Li/Mg–dual-ion electrode. Compared to defect-free TiO_2, the presence of cationic vacancies gives an improved reversible capacity, a reduced polarization, and a higher operating voltage, leading to an overall increase of the cell energy density. The number of inserted cations was determined by ICP-AES confirming a dual-ion insertion into the host electrode structure. Pair distribution function confirmed that the long-range ordering of the anatase framework is maintained upon dual-insertion, also pointing the occurrence of local distortion. Solid-state NMR further proved the insertion of both ions within the vacant sites. DFT-calculations highlighted the lithium-concentration dependence on the population of the available vacant sites. It also showed that the double-vacancy insertion properties are significantly impact by the nature of the first-inserted cation, in particular with the strongly polarizing Mg^{2+} cations. The improvements in electrode performance described here suggest that

this approach can be beneficially extended to other electrode materials and other types of dual-ion battery systems.

Experimental Section

Synthesis: anatase $Ti_{0.78}\square_{0.22}O_{1.12}F_{0.40}(OH)_{0.48}$ was synthesized according to a previous report.[17] Briefly, 1.2 mL aqueous hydrofluoric acid solution was added to the mixture of 24.8 mL isopropanol and 4 mL titanium isopropoxide in the Teflon liner cup. A stainless-steel autoclave with a 45 mL Teflon liner cup inside was used. After sealing the autoclave, the mixed solution was heated inside an oven at 90 °C for 12 h, and left to cool down to room temperature. The resulting white precipitate was recovered, then first dried at 80 °C under air for 10 h and at 150 °C under vacuum for 10 hours.

Characterization methods: Inductively coupled plasma atomic emission spectrometry (ICP-AES) was measured on Agilent Varian 715-ES to assess the chemical composition of discharged–charged electrodes. Samples were dissolved by microwave digestion at 180 °C into acidic solutions of HNO_3, H_2SO_4, and HCl (1:1:3 vol.%). Total scattering data were collected at the 11-ID-B beamline at the Advanced Photon Source at Argonne National Laboratory, using high energy X-rays (λ = 0.2128 Å) for high values of momentum transfer Qmax = 22 $Å^{-1}$.[40,41] One-dimensional diffraction data were obtained by integrating the raw 2D total scattering data in Fit2D.[42] PDFs, G(*r*), were extracted from the background and Compton scattering corrected data following Fourier transform within PDFgetX2.[43] The PDFs were subsequently modeled using PDFgui.[44] The Q_{damp} was fixed to 0.04. The structural model used was tetragonal anatase (space group $I4_1/amd$). The refined parameters includes lattice parameters, scale factor, *s*ratio (*i.e.* low-*r* to high-*r* PDF peak ratio correction due to the correlated motion of bonded atoms[45]), spdiameter (*i.e.* particle diameter), and isotropic atomic displacement factors (ADPs).

The quality of the refinement is quantified by the reliability factor weighted R-value, denoted as R_w. The R-value describes the difference between the experimental observation (data) and the calculated value (fit) for a single data point. The R_w is the R-value weighted for data point *i*, and is given by the formula:

$$R_w = \sqrt{\frac{\sum_{i=1}^{N} w(r_i)[G_{obs}(r_i) - G_{calc}(r_i)]^2}{\sum_{i=1}^{N} w(r_i) G_{obs}^2(r_i)}}$$

with G_{obs} and G_{calc} being the observed (data) and calculated (fit) PDF and $w(r_i)$ the weight for each data point.

^{19}F and ^{7}Li Solid-State NMR Spectroscopy. ^{19}F and ^{7}Li solid-state magic angle spinning (MAS) NMR experiments were performed on a Bruker Avance 300 spectrometer operating at 7.0 T (^{19}F and ^{7}Li Larmor frequencies of 282.2 and 116.7 MHz, respectively), using a 1.3 mm CP-MAS probe head. The electrochemically prepared samples were washed with DMF and stored under dry nitrogen gas, in a glove box, in which the 1.3 mm rotors have been filled. Experimental details about the ^{19}F MAS NMR spectrum of $Ti_{0.78}\square_{0.22}O_{1.12}F_{0.40}(OH)_{0.48}$ have been reported previously.[17] The room temperature ^{19}F MAS spectra of the electrochemically prepared samples (charged and discharged electrodes) were recorded using a Hahn echo sequence with an interpulse delay equal to one rotor period. The 90° pulse length was set to 1.25 μs, and the recycle delay was set to 10 or 20 s. The room temperature ^{7}Li MAS spectra of the charged and discharged electrodes were recorded using a single pulse sequence. The 90° pulse length was set to 2 μs, and the recycle delay was set to 10 s or 30 s. ^{19}F and ^{7}Li spectra are referenced to $CFCl_3$ and 1 M LiCl aqueous solution, respectively, and they were fitted by using the DMFit software.[46]

Electrochemistry: The composition of the electrode was 80 wt.% active materials, 10 wt.% C (Timcal, Super P), and 10 wt.% polyvinylidene difluoride (PVDF, Aldrich). The electrode materials were drop-coated on a Mo foil (≥99.9%, Aldrich)[19] with the density of 2 mg cm^{-2}. 0.2 M APC + LiCl / THF was prepared by mixing 2 M PhMgCl / THF (Sigma-Aldrich) and 0.5 M $AlCl_3$ / THF (Sigma-Aldrich) in THF (anhydrous, ≥99.9%, Sigma-Aldrich) dropwise under stirring for 12 hours. LiCl (ultra-dry, 99.995%, Alfa Aesar) was further added under stirring condition, and stirred for at least 12 hours. Borosilicate glass-fiber separator (Whatmann Grade GF/D) was soaked with 400 μL of the electrolyte solution. Mg metal was used as the counter and reference electrodes. Electrochemical measurements were carried out using three-electrode Swagelok-type cells within the voltage range of 0.05 – 2.3 V *vs.* Mg^{2+}/Mg, and the temperature was set at 25 $^{\circ}$C using a thermostatic chamber. The cells were assembled in an argon-filled glovebox, and the data was collected on SP-200 or BCS-805 (Bio-Logic Science Instruments). Galvanostatic-intermittent-titration-technique was applied during the first discharge. A constant-current discharge pulse at the current density of 10 mA g^{-1} was applied to the cell for 1 h, followed by a relaxation period for 10 h. This protocol was repeated until the cell potential reached +0.05 V vs. Mg^{2+}/Mg.

Computational: We performed our density functional theory calculations using the code VASP[47,48], with valence electrons described by a plane-wave basis with a cutoff of 500 eV. Interactions between core and valence electrons were described using the projector augmented wave (PAW) method[49], with cores of [Mg] for Ti, [He] for O, [He] for F, [H^+] for Li, [He] for Mg, and [H^+] for H. The calculations used the revised Perdew-Burke-Ernzerhof generalized gradient approximation function PBEsol,[50] with a Dudarev +*U* correction applied to the Ti d states (GGA+*U*).[51,52] We used a value of $U_{\mathrm{Ti},d} = 4.2$ eV, which has previously been used to

model intercalation of lithium and other metal ions in anatase TiO_2 and TiO_2(B).[16,23,52,53] To model anatase TiO_2, we first performed a full geometry optimisation on a single Ti_4O_8 unit cell, with optimized lattice parameters obtained by fitting a series of constant volume calculations to the Murnaghan equation of state. All subsequent calculations were fixed to the resulting optimised lattice parameters. Intercalation into stoichiometric anatase TiO_2 was modelled using a 4 × 4 × 2 supercell (384 atoms), with a single Li ion inserted at an interstitial site ($LiTi_{128}O_{256}$). To model intercalation at single- and double-titanium vacancies we performed a series of calculations in 4 × 4 × 2 supercells, with either 1 Ti vacancy, and 4 charge compensating F anions, giving cell stoichiometries of $Ti_{127}O_{252}F_4$, or 2 Ti vacancies, and 8 charge compensating F anions, giving a stoichiometry of $Ti_{126}O_{248}F_8$. In both cases, we consider models with all fluoride ions occupying anion sites adjacent to the titanium vacancies, which we have previously shown minimizes the DFT-calculated energy.[17,26,32]

Individual calculations were deemed optimized when all atomic forces were smaller than 0.01 eV $Å^{-1}$. All calculations were spin polarized, and used a 2 × 2 × 2 Monkhorst-Pack grid for sampling *k*-space. To calculate intercalation energies, reference calculations for metallic Li and metallic Mg were performed using the same convergence criteria as above. For both metals we considered 2-atom cells, and used a 16 × 16 × 16 Monkhorst-Pack grid for Li and a 18 × 18 × 18 Monkhorst-Pack grid for Mg for *k*-space sampling. A data set containing all DFT calculation inputs and outputs is available at the University of Bath Data Archive, published under the CC-BY-4.0 license.[39] The dataset also includes analysis scripts, published under the MIT license, used to post-process the DFT data and to generate **Fig. 6**. The data analysis scripts use the Python packages numpy,[54,55] snakemake,[56] surfinpy,[57] and vasppy.[58]

Supporting Information
Supporting Information file.

Acknowledgements

The research leading to these results has received funding from the French National Research Agency under Idex@Sorbonne University for the Future Investments program (No. ANR-11-IDEX-0004-02) and "Sino German TU9 network for electromobility" under the grant reference number 16N11929. The work done at the Advanced Photon Source, an Office of Science User Facility operated for the U. S. Department of Energy (DOE) Office of Science by Argonne National Laboratory, was supported by the U.S. DOE under Contract No. DE-AC02-06CH11357. B. J. M. acknowledges support from the Royal Society (Grant No. UF130329), and the Faraday Institution (faraday.ac.uk; EP/S003053/1, grant number FIRG003). Calculations were performed using the Balena High Performance Computing Service at the University of Bath, and the ARCHER supercomputer, through membership of the UK's HPC Materials Chemistry Consortium, funded by EPSRC grant EP/L000202.

References

[1] B. Dunn, H. Kamath, J.-M. Tarascon, Electrical Energy Storage for the Grid: A Battery of Choices, Science. 334 (2011) 928–935. doi:10.1126/science.1212741.

[2] D. Aurbach, Z. Lu, A. Schechter, Y. Gofer, H. Gizbar, R. Turgeman, Y. Cohen, M. Moshkovich, E. Levi, Prototype systems for rechargeable magnesium batteries, Nature. 407 (2000) 724–727. doi:10.1038/35037553.

[3] D. Aurbach, Y. Cohen, M. Moshkovich, The Study of Reversible Magnesium Deposition by In Situ Scanning Tunneling Microscopy, Electrochem. Solid-State Lett. 4 (2001) A113–A116. doi:10.1149/1.1379828.

[4] M. Matsui, Study on electrochemically deposited Mg metal, Journal of Power Sources. 196 (2011) 7048–7055. doi:10.1016/j.jpowsour.2010.11.141.

[5] H.D. Yoo, I. Shterenberg, Y. Gofer, G. Gershinsky, N. Pour, D. Aurbach, Mg rechargeable batteries: an on-going challenge, Energy Environ. Sci. 6 (2013) 2265–2279. doi:10.1039/C3EE40871J.

[6] X. Sun, P. Bonnick, V. Duffort, M. Liu, Z. Rong, K.A. Persson, G. Ceder, L.F. Nazar, A high capacity thiospinel cathode for Mg batteries, Energy Environ. Sci. 9 (2016) 2273–2277. doi:10.1039/C6EE00724D.

[7] X. Sun, P. Bonnick, L.F. Nazar, Layered TiS2 Positive Electrode for Mg Batteries, ACS Energy Lett. 1 (2016) 297–301. doi:10.1021/acsenergylett.6b00145.

[8] V. Duffort, X. Sun, L.F. Nazar, Screening for positive electrodes for magnesium batteries: a protocol for studies at elevated temperatures, Chem. Commun. 52 (2016) 12458–12461. doi:10.1039/C6CC05363G.

[9] M. Liu, Z. Rong, R. Malik, P. Canepa, A. Jain, G. Ceder, K. A. Persson, Spinel compounds as multivalent battery cathodes: a systematic evaluation based on ab initio calculations, Energy & Environmental Science. 8 (2015) 964–974. doi:10.1039/C4EE03389B.

[10] Z. Rong, R. Malik, P. Canepa, G. Sai Gautam, M. Liu, A. Jain, K. Persson, G. Ceder, Materials Design Rules for Multivalent Ion Mobility in Intercalation Structures, Chem. Mater. 27 (2015) 6016–6021. doi:10.1021/acs.chemmater.5b02342.

[11] Z. Rong, P. Xiao, M. Liu, W. Huang, D.C. Hannah, W. Scullin, K.A. Persson, G. Ceder, Fast Mg2+ diffusion in Mo3(PO4)3O for Mg batteries, Chem. Commun. 53 (2017) 7998–8001. doi:10.1039/C7CC02903A.
[12] J.-H. Cho, M. Aykol, S. Kim, J.-H. Ha, C. Wolverton, K.Y. Chung, K.-B. Kim, B.-W. Cho, Controlling the Intercalation Chemistry to Design High-Performance Dual-Salt Hybrid Rechargeable Batteries, J. Am. Chem. Soc. 136 (2014) 16116–16119. doi:10.1021/ja508463z.
[13] Y. Gofer, O. Chusid, H. Gizbar, Y. Viestfrid, H.E. Gottlieb, V. Marks, D. Aurbach, Improved Electrolyte Solutions for Rechargeable Magnesium Batteries, Electrochem. Solid-State Lett. 9 (2006) A257–A260. doi:10.1149/1.2186003.
[14] T. Ichitsubo, S. Okamoto, T. Kawaguchi, Y. Kumagai, F. Oba, S. Yagi, N. Goto, T. Doi, E. Matsubara, Toward "rocking-chair type" Mg–Li dual-salt batteries, J. Mater. Chem. A. 3 (2015) 10188–10194. doi:10.1039/C5TA01365H.
[15] H. Li, N.L. Okamoto, T. Hatakeyama, Y. Kumagai, F. Oba, T. Ichitsubo, Fast Diffusion of Multivalent Ions Facilitated by Concerted Interactions in Dual-Ion Battery Systems, Advanced Energy Materials. 8 (2018) 1801475. doi:10.1002/aenm.201801475.
[16] T. Koketsu, J. Ma, B.J. Morgan, M. Body, C. Legein, W. Dachraoui, M. Giannini, A. Demortière, M. Salanne, F. Dardoize, H. Groult, O.J. Borkiewicz, K.W. Chapman, P. Strasser, D. Dambournet, Reversible magnesium and aluminium ions insertion in cation-deficient anatase TiO_2, Nature Materials. 16 (2017) 1142. doi:10.1038/nmat4976.
[17] W. Li, D. Corradini, M. Body, C. Legein, M. Salanne, J. Ma, K.W. Chapman, P.J. Chupas, A.-L. Rollet, C. Julien, K. Zhagib, M. Duttine, A. Demourgues, H. Groult, D. Dambournet, High Substitution Rate in TiO2 Anatase Nanoparticles with Cationic Vacancies for Fast Lithium Storage, Chem. Mater. 27 (2015) 5014–5019. doi:10.1021/acs.chemmater.5b01407.
[18] H.D. Yoo, Y. Liang, Y. Li, Y. Yao, High Areal Capacity Hybrid Magnesium–Lithium-Ion Battery with 99.9% Coulombic Efficiency for Large-Scale Energy Storage, ACS Appl. Mater. Interfaces. 7 (2015) 7001–7007. doi:10.1021/acsami.5b01206.
[19] M. Wagemaker, W.J.H. Borghols, F.M. Mulder, Large Impact of Particle Size on Insertion Reactions. A Case for Anatase LixTiO2, J. Am. Chem. Soc. 129 (2007) 4323–4327. doi:10.1021/ja067733p.
[20] S. Sodergren, H. Siegbahn, H. Rensmo, H. Lindstrom, A. Hagfeldt, S.E. Lindquist, Lithium intercalation in nanoporous anatase TiO2 studied with XPS, J. Phys. Chem. B. 101 (1997) 3087–3090. doi:10.1021/jp9639399.
[21] High catalytic activity of anatase titanium dioxide for decomposition of electrolyte solution in lithium ion battery - ScienceDirect, (n.d.). https://www.sciencedirect.com/science/article/pii/S0378775314009306 (accessed September 18, 2019).
[22] W. Weppner, R.A. Huggins, Determination of the Kinetic Parameters of Mixed-Conducting Electrodes and Application to the System Li3Sb, J. Electrochem. Soc. 124 (1977) 1569–1578. doi:10.1149/1.2133112.
[23] B.J. Morgan, G.W. Watson, Role of Lithium Ordering in the LixTiO2 Anatase → Titanate Phase Transition, J. Phys. Chem. Lett. 2 (2011) 1657–1661. doi:10.1021/jz200718e.
[24] A.A. Belak, Y. Wang, A. Van der Ven, Kinetics of Anatase Electrodes: The Role of Ordering, Anisotropy, and Shape Memory Effects, Chem. Mater. 24 (2012) 2894–2898. doi:10.1021/cm300881t.

[25] P.L. Taberna, S. Mitra, P. Poizot, P. Simon, J.-M. Tarascon, High rate capabilities Fe_3O_4-based Cu nano-architectured electrodes for lithium-ion battery applications, Nature Materials. 5 (2006) 567–573. doi:10.1038/nmat1672.
[26] J. Ma, T. Koketsu, B.J. Morgan, C. Legein, M. Body, P. Strasser, D. Dambournet, Controlled hydroxy-fluorination reaction of anatase to promote Mg2+ mobility in rechargeable magnesium batteries, Chem. Commun. 54 (2018) 10080–10083. doi:10.1039/C8CC04136A.
[27] D.A. Keen, A comparison of various commonly used correlation functions for describing total scattering, J Appl Cryst, J Appl Crystallogr. 34 (2001) 172–177. doi:10.1107/S0021889800019993.
[28] S.J.L. Billinge, I. Levin, The Problem with Determining Atomic Structure at the Nanoscale, Science. 316 (2007) 561–565. doi:10.1126/science.1135080.
[29] M. Wagemaker, G.J. Kearley, A.A. van Well, H. Mutka, F.M. Mulder, Multiple Li Positions inside Oxygen Octahedra in Lithiated TiO2 Anatase, J. Am. Chem. Soc. 125 (2003) 840–848. doi:10.1021/ja028165q.
[30] K. Shen, H. Chen, F. Klaver, F.M. Mulder, M. Wagemaker, Impact of Particle Size on the Non-Equilibrium Phase Transition of Lithium-Inserted Anatase TiO2, Chem. Mater. 26 (2014) 1608–1615. doi:10.1021/cm4037346.
[31] A. Sadoc, M. Body, C. Legein, M. Biswal, F. Fayon, X. Rocquefelte, F. Boucher, NMR parameters in alkali, alkaline earth and rare earth fluorides from first principle calculations, Phys. Chem. Chem. Phys. 13 (2011) 18539–18550. doi:10.1039/C1CP21253B.
[32] J. Ma, W. Li, B.J. Morgan, J. Światowska, R. Baddour-Hadjean, M. Body, C. Legein, O.J. Borkiewicz, S. Leclerc, H. Groult, F. Lantelme, C. Laberty-Robert, D. Dambournet, Lithium Intercalation in Anatase Titanium Vacancies and the Role of Local Anionic Environment, Chem. Mater. 30 (2018) 3078–3089. doi:10.1021/acs.chemmater.8b00925.
[33] R.J. Messinger, M. Ménétrier, E. Salager, A. Boulineau, M. Duttine, D. Carlier, J.-M. Ateba Mba, L. Croguennec, C. Masquelier, D. Massiot, M. Deschamps, Revealing Defects in Crystalline Lithium-Ion Battery Electrodes by Solid-State NMR: Applications to $LiVPO_4F$, Chem. Mater. 27 (2015) 5212–5221. doi:10.1021/acs.chemmater.5b01234.
[34] V. Luca, T.L. Hanley, N.K. Roberts, R.F. Howe, NMR and X-ray Absorption Study of Lithium Intercalation in Micro- and Nanocrystalline Anatase, Chem. Mater. 11 (1999) 2089–2102. doi:10.1021/cm990007j.
[35] M. Wagemaker, R. van de Krol, A.P.M. Kentgens, A.A. van Well, F.M. Mulder, Two Phase Morphology Limits Lithium Diffusion in TiO_2 (Anatase): A ^{7}Li MAS NMR Study, J. Am. Chem. Soc. 123 (2001) 11454–11461. doi:10.1021/ja0161148.
[36] A.Y.H. Lo, R.W. Schurko, M. Vettraino, B.O. Skadtchenko, M. Trudeau, D.M. Antonelli, Solid-State ^{23}Na and ^{7}Li NMR Investigations of Sodium- and Lithium-Reduced Mesoporous Titanium Oxides, Inorg. Chem. 45 (2006) 1828–1838. doi:10.1021/ic051654h.
[37] H. Günther, Lithium NMR, in: R.K. Harris (Ed.), Encyclopedia of Magnetic Resonance, John Wiley & Sons, Ltd, Chichester, UK, 2007: p. emrstm0273. doi:10.1002/9780470034590.emrstm0273.
[38] M.K. Aydinol, A.F. Kohan, G. Ceder, K. Cho, J. Joannopoulos, Ab initio study of lithium intercalation in metal oxides and metal dichalcogenides, Phys. Rev. B. 56 (1997) 1354–1365. doi:10.1103/PhysRevB.56.1354.

[39] Morgan, B. DFT dataset: Exploiting Cationic Vacancies for Increased Energy Densities in Dual-Ion Batteries; University of Bath Research Data Archive, 2019. doi.org/10.15125/BATH-00689
[40] P.J. Chupas, X. Qiu, J.C. Hanson, P.L. Lee, C.P. Grey, S.J.L. Billinge, Rapid-acquisition pair distribution function (RA-PDF) analysis, Journal of Applied Crystallography. 36 (2003) 1342–1347. doi:10.1107/S0021889803017564.
[41] P.J. Chupas, K.W. Chapman, P.L. Lee, Applications of an amorphous silicon-based area detector for high-resolution, high-sensitivity and fast time-resolved pair distribution function measurements, Journal of Applied Crystallography. 40 (2007) 463–470. doi:10.1107/S0021889807007856.
[42] A.P. Hammersley, S.O. Svensson, M. Hanfland, A.N. Fitch, D. Hausermann, Two-dimensional detector software: From real detector to idealised image or two-theta scan, High Pressure Research. 14 (1996) 235–248. doi:10.1080/08957959608201408.
[43] X. Qiu, J.W. Thompson, S.J.L. Billinge, PDFgetX2: a GUI-driven program to obtain the pair distribution function from X-ray powder diffraction data, J. Appl. Cryst. 37 (2004) 678–678. doi:10.1107/S0021889804011744.
[44] C.L. Farrow, P. Juhas, J.W. Liu, D. Bryndin, E.S. Božin, J. Bloch, T. Proffen, S.J.L. Billinge, PDFfit2 and PDFgui: computer programs for studying nanostructure in crystals, Journal of Physics: Condensed Matter. 19 (2007) 335219. doi:10.1088/0953-8984/19/33/335219.
[45] T. Egami, S.J.L. Billinge, Underneath the Bragg Peaks: Structural Analysis of Complex Materials, Elsevier, 2003.
[46] D. Massiot, F. Fayon, M. Capron, I. King, S. Le Calvé, B. Alonso, J.-O. Durand, B. Bujoli, Z. Gan, G. Hoatson, Modelling one- and two-dimensional solid-state NMR spectra, Magn. Reson. Chem. 40 (2002) 70–76. doi:10.1002/mrc.984.
[47] G. Kresse, J. Hafner, Norm-conserving and ultrasoft pseudopotentials for first-row and transition elements, J. Phys.: Condens. Matter. 6 (1994) 8245. doi:10.1088/0953-8984/6/40/015.
[48] G. Kresse, J. Furthmüller, Efficiency of ab-initio total energy calculations for metals and semiconductors using a plane-wave basis set, Computational Materials Science. 6 (1996) 15–50. doi:10.1016/0927-0256(96)00008-0.
[49] G. Kresse, D. Joubert, From ultrasoft pseudopotentials to the projector augmented-wave method, Phys. Rev. B. 59 (1999) 1758–1775. doi:10.1103/PhysRevB.59.1758.
[50] S.L. Dudarev, A.I. Liechtenstein, M.R. Castell, G.A.D. Briggs, A.P. Sutton, Surface states on NiO (100) and the origin of the contrast reversal in atomically resolved scanning tunneling microscope images, Phys. Rev. B. 56 (1997) 4900–4908. doi:10.1103/PhysRevB.56.4900.
[51] S.L. Dudarev, G.A. Botton, S.Y. Savrasov, C.J. Humphreys, A.P. Sutton, Electron-energy-loss spectra and the structural stability of nickel oxide: An LSDA+U study, Phys. Rev. B. 57 (1998) 1505–1509. doi:10.1103/PhysRevB.57.1505.
[52] B.J. Morgan, G.W. Watson, $\text{GGA}+U$ description of lithium intercalation into anatase ${\text{TiO}}_{2}$, Phys. Rev. B. 82 (2010) 144119. doi:10.1103/PhysRevB.82.144119.
[53] B.J. Morgan, P.A. Madden, Lithium intercalation into TiO${}_{2}$(B): A comparison of LDA, GGA, and GGA+U density functional calculations, Phys. Rev. B. 86 (2012) 035147. doi:10.1103/PhysRevB.86.035147.

[54] T.E. Oliphant, Guide to NumPy, 2nd ed., CreateSpace Independent Publishing Platform, USA, 2015.
[55] S. van der Walt, S.C. Colbert, G. Varoquaux, The NumPy Array: A Structure for Efficient Numerical Computation, Computing in Science Engineering. 13 (2011) 22–30. doi:10.1109/MCSE.2011.37.
[56] J. Köster, S. Rahmann, Snakemake—a scalable bioinformatics workflow engine, Bioinformatics. 28 (2012) 2520–2522. doi:10.1093/bioinformatics/bts480.
[57] surfinpy: A Surface Phase Diagram Generator, The Journal of Open Source Software. (2019). doi:10.21105/joss.01210.
[58] B.J. Morgan, vasppy, Zenodo, 2019. doi:10.5281/zenodo.2667551.

Graphical abstract